



Functional AlF_3 modification over 5 V spinel LiCoMnO_4 cathode for Li-ion batteries

Sreekumar Sreedeeep^a, Yun-Sung Lee^{b,*}, Vanchiappan Aravindan^{a,**}

^a Department of Chemistry, Indian Institute of Science Education and Research (IISER), Tirupati, 517507, India

^b School of Chemical Engineering, Chonnam National University, Gwang-ju, 61186, Republic of Korea

ARTICLE INFO

Handling editor: Prof. Joong Lee

Keywords:

High voltage cathode

LiCoMnO_4

AlF_3 coating

Full-cell

$\text{Li}_4\text{Ti}_5\text{O}_{12}$ anode

ABSTRACT

We report the improved electrochemical activity of the 5 V LiCoMnO_4 (LCMO) cathode with the functionalization of AlF_3 coating. LCMO@AlF_3 is prepared by adopting the co-precipitation technique followed by a wet coating by altering the concentration of AlF_3 by 1–3 wt.%. LCMO@AlF_3 exhibits improvement in the electrochemical performance compared to pristine LCMO. In addition, LCMO@AlF_3 exhibits superior electrochemical performance with specific capacities of 107, 102, and 95 mAh g^{-1} and retentions of 68, 77, and 74% after 100 cycles for 1, 2, and 3 wt.% AlF_3 coating. However, pristine LCMO shows a specific capacity of 105 mAh g^{-1} with a retention of 48% after 100 cycles. Also, LCMO@AlF_3 exhibits a decrement in the irreversible capacity loss (ICL) compared to pristine LCMO, which enhances the coulombic efficiency of the former compared to the latter. Further, the AlF_3 coating of 2 and 3 wt.% has been optimized to exhibit excellent electrochemical performance. The diffusion coefficients are calculated from cyclic voltammetric and electrochemical impedance spectroscopic techniques and are in the order of $\sim 10^{-12} \text{ cm}^2 \text{ s}^{-1}$. Further, *in-operando* and *in-situ* impedance studies are conducted to authenticate the electrochemical activity observed in half-cell studies. In full-cell assembly with $\text{Li}_4\text{Ti}_5\text{O}_{12}$ (LTO) anode, the LCMO@AlF_3 : 2–3 wt.% exhibits better electrochemical performance compared to its bare configuration. In addition, the electrochemical activity at various temperature (–10 to 25 °C) conditions is performed and reported.

1. Introduction

The ever-growing rise in fossil fuel usage, global warming, and environmental pollution are the major threats the modern world is facing. The over-exploitation of fossil fuels has led to a drastic decrease in their availability from the earth's crest. Therefore, overcoming the current energy scenario with a more eco-friendly and sustainable energy technology has become one of the primary concerns confronted by the scientific community. Hence, the development of energy storage devices, predominantly batteries, has gained much attention. Among the various battery technologies developed so far, the advent of Lithium-ion batteries (LIBs) created a breakthrough in science and technology owing to their high energy density, shape versatility, and low safety limits, which made it applied in wide areas, including portable electronic devices, grid applications, and emission-free transportation like electric and hybrid electric vehicles (EV and HEVs) [1,2]. Therefore, to cope with the current demand for LIBs, there is an urgent need to enhance the

energy density of the batteries [3–6]. As the energy density depends on the specific capacity and cell voltage, an increase in either one of the parameters can enhance the same. However, the limited scope of enhancing the specific capacity of the cell finally deviated towards enhancing the cell voltage. However, among the various components of the battery, the cathode plays a dominant role in improving the cell voltage, hence the energy density [7].

The recent year marks the development of various high-voltage cathodes ($>4.5 \text{ V vs. Li/Li}^+$) with excellent electrochemical properties. The various high-voltage cathodes in the development stage include Li-rich layered oxides ($\text{Li}_{1+x}\text{M}_{1-x}\text{O}_2$, M: Co, Mn, Al), spinel oxides, and polyanionic compounds (phosphates, sulfates) that have an average working voltage close to 4.5 V vs. Li/Li^+ or below [7,8]. However, the development of $>4.5 \text{ V vs. Li/Li}^+$ cathode materials remains one of the greatest challenges that must be resolved. Even though cathodes such as olivine type LiCoPO_4 and spinel $\text{LiNi}_{0.5}\text{Mn}_{1.5}\text{O}_4$ gained attention as 5 V vs. Li/Li^+ class cathodes, both have an average working voltage close to

* Corresponding author.

** Corresponding author.

E-mail addresses: leeys@chonnam.ac.kr (Y.-S. Lee), aravind.van@gmail.com (V. Aravindan).

4.8 V vs. Li/Li⁺ [9–11]. The spinel, cubic phased LiCoMnO₄, owing to the high specific capacity of 145 mAh g⁻¹ and working voltage of 5 V vs. Li/Li⁺, has become a promising candidate among the high-voltage cathodes for LIB applications [12–18]. It also exhibits a very low volume change of 0.7% during charge-discharge, making it dimensionally more stable. Although exhibiting the desirable features of an excellent cathode, the commercialization of LiCoMnO₄ is hindered by the poor coulombic efficiency, rapid capacity fade, and coexistence of insulating Li₂MnO₃ phase [19]. Hence, strategies have to be implemented to improve the electrochemical performance of LiCoMnO₄.

To improve the electrochemical properties of the LiCoMnO₄ cathode, various strategies have to be implemented, including surface modification. Based on the nature of coating materials, the method of surface modification can be broadly classified into inorganic-based (oxide, fluorides) [8,20], carbon-based [20–23], and polymer-based material (PANI, PEDOT) [24,25] coating. The surface modification process enhances the electronic and Li⁺ ion conduction, protects the cathode from undesirable parasitic reactions, and prevents the transition metal dissolution, improving the rate capability and the electrochemical performance. Zhao *et al.* [26] observed that the LiF/FeF₃ protective coating on Li [Li_{0.2}Ni_{0.2}Mn_{0.6}]O₂ had enhanced its electrochemical performance. In addition, Lee *et al.* [27] showed that the ZrO₂ surface coating on Li [Li_{0.2}Ni_{0.2}Mn_{0.6}]O₂ had enhanced the cycle stability as well as the rate capability of the material. Although an increase in the electrochemical properties has been observed upon surface modification, it doesn't mean that increasing the coating percentage will give a proportional increase in the electrochemical properties. Hence, optimizing the coating percentage is also much more important.

An *ex-situ* AlF₃ surface coating has been adopted over LCMO particles to eliminate the setbacks. Generally, AlF₃ coating imparts high ionic conductivity and good electrochemical stability due to a stable Al–F bond [28,29]. In addition, the *in-situ* XRD and EIS analyses have been performed to understand the redox reaction observed during the charge-discharge studies along with phase transition. Finally, the full-cell assembly was done with another spinel anode, Li₄Ti₅O₁₂, and its performance in various climatic conditions was studied and reported.

2. Experimental section

2.1. Synthesis

The synthesis of LiCoMnO₄ was carried out by a co-precipitation method. The precursors of the cathode material, Co(CH₃COO)₂·4H₂O (Sigma-Aldrich, ≥98%) and Mn(CH₃COO)₂·4H₂O (Sigma-Aldrich, ≥99%), were taken in a stoichiometric amount, and are dissolved in deionized water under magnetic stirring, followed by the addition of 30 ml of ethanol. The precipitation was initiated by adding a stoichiometric amount of (NH₄)₂CO₃ to the precursor solution. The precipitate was allowed to settle down, washed with distilled water and ethanol, and dried at room temperature. The as-obtained precursor was then calcined in air at 400 °C for 5 h. The above-obtained sample was mixed with a stoichiometric amount of CH₃COOLi (Sigma-Aldrich, 99.95%), followed by calcination in Argon atmosphere at 800 °C for 5 h.

2.2. AlF₃ coating

To synthesize AlF₃-coated LCMO, the as-prepared LCMO was dispersed in an aqueous solution containing Al(NO₃)₃·9H₂O (Sigma Aldrich, ≥98%) followed by drop-wise addition of NH₄F (Sigma Aldrich, ≥99.99%) till the molar ratio of Al to F was achieved. Now, the solution was kept in an oven for the water to get evaporated. The obtained dried sample was now calcined to a temperature of 400 °C for 2 h in an argon atmosphere. The LCMO with different AlF₃ loading, denoted as LCMO@AlF₃- 1 wt.%, LCMO@AlF₃- 2 wt.%, and LCMO@AlF₃- 3 wt.% was prepared, and their electrochemical study were carried out.

2.3. Electrolyte preparation

The electrolyte preparation was carried out in an Ar-filled Glove box using 1 M LiPF₆ dissolved in Ethylene carbonate (EC) and Dimethyl carbonate (DMC) (1:1 wt ratio, LIPASTE, Tomiyama), with the addition of Fluoroethylene carbonate (FEC) (Sigma Aldrich, ≥99%) as an electrolyte additive (10 wt.%).

2.4. Electrochemical characterization

The working electrode has been made by mixing 10 mg of active material (LCMO@AlF₃: 1–3 wt.%), 2 mg of conductive additive (Acetylene black), and 2 mg of binder (Teflonized acetylene black-2, TAB) into a free-standing film using ethanol as the medium. The electrode was vacuum-dried overnight to remove the moisture content, and the cell was fabricated in an Ar-filled Glove box (MBraun, Germany) in a CR2016 coin cell with a glass microfiber separator (Whatman, 1825–047, UK). The coin cell was subjected to preliminary studies within a 3.5 and 5.2 V voltage range in half-cell assembly.

The full cell has been fabricated with Li₄Ti₅O₁₂ (LTO) as the counter electrode. The LTO electrode has been made by preparing a homogenous slurry by mixing the active material (LTO), conductive carbon (Acetylene black, AB), and binder (PVDF) in a weight ratio of 80:10:10 in N-methyl-2-pyrrolidone (NMP). The electrodes were made by coating the slurry on an Al-foil using a doctor blade setup and were cut into 14 mm diameter circular electrodes. The electrodes are then kept in a vacuum oven to remove the moisture. The full cell fabrication has been done by combining the LCMO@AlF₃ electrodes along with LTO in an Ar-filled Glove box. Now, the full cell study has been carried out in a battery tester (Biologic, France) within a voltage range of 1.5 and 3.7 V. Along with that, the temperature study of the same has been carried out in an environmental chamber (Espec, Japan) within a range of –10 to 20 °C.

2.5. Material characterization

The structural characterization of the as-prepared LCMO@AlF₃: 1–3 wt.% has been carried out using an X-ray Diffraction analysis (XRD, Rigaku, Smart lab 9 kW, monochromatic Cu Kα radiation (λ = 1.5406 Å)) at a scan rate of 0.1° min⁻¹ within a 2θ range of 10 to 80°. The elemental analysis, as well as the chemical state of the elements, have been determined from X-ray Photoelectron spectroscopy (XPS, with a multilab instrument with a monochromatic Al Kα radiation hv = 1486.6 eV). In addition, the Raman spectroscopy (LabRam HR800 UV Raman microscope, Horiba Jobin-Yvon, France) of the material has been done. The morphology and shape of the material have been analyzed from the FE-SEM (S-4700, Hitachi, Japan) and HR-TEM (TECNAL, Philips, the Netherlands, 200 keV) analysis. Also, the homogeneity of the elemental distribution was analyzed using the EDS analysis of the material.

3. Results and discussion

The structural elucidation of pristine LCMO and the LCMO@AlF₃: 1–3 wt.% using powder XRD analysis (Fig. 1) reveals the formation of a cubic phase with an Fd3m space group. Moreover, the crystalline nature of the sample has been confirmed by the strong and sharp reflections of (111), (311), (400), and (440) planes. Also, the absence of AlF₃ diffraction peaks accounts for the low concentration of AlF₃ in the sample. The functional group analysis using IR spectroscopy (Fig. S1) indicates the presence of Mn–O and Co–O at 652 and 525 cm⁻¹, respectively. The Raman spectra (Fig. S2) indicate the presence of an Fd3m space group, which agrees with the XRD analysis. Also, the more intense band at 630 cm⁻¹ (A_g) corresponds to the Mn–O vibration, and the less intense band at 694 cm⁻¹ is assigned to the Co–O stretching vibration, respectively [29–31]. The XPS analysis (Fig. 2(a–f)) performed for the as-synthesized LCMO@AlF₃ shows the existence of elements such as Li, Co, Mn, O, and C in the compound, while the chemical

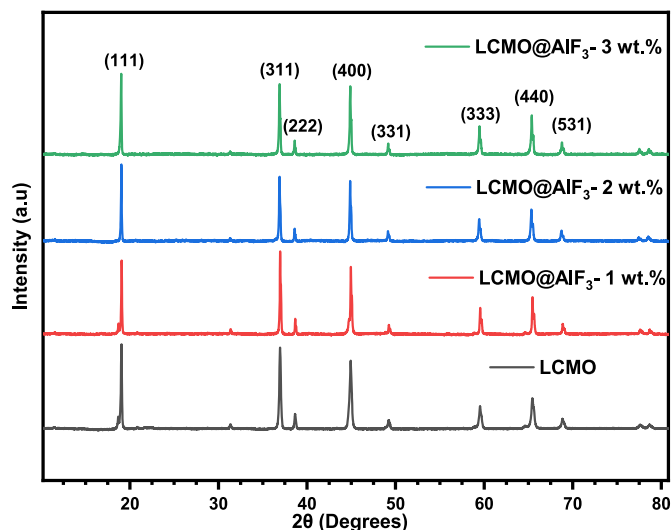


Fig. 1. XRD pattern of pristine LCMO and LCMO@AlF₃: 1–3 wt.%.

state of these elements has been evaluated to be Li 1s, Al 2p, Co 2p, Mn 2p, O 1s, C 1s, and F 1s. In addition, the oxidation state of the transition metals Mn 2p and Co 2p has been evaluated to be +4 and +3, consistent with the previous reports [32].

The XPS spectra of F 1s exhibit a broad single peak of C–F at 688.7 eV, along with the peak at 75 eV showing the Al–F bond, hence confirming the presence of AlF₃ coating on the sample. In addition, O 1s spectra exhibit peaks indicating the presence of MO (Co–O, Mn–O), C–O, and C=O at binding energies of 529.8, 531.9, and 533.8 eV, respectively. Meanwhile, the C 1s spectra exhibit peaks indicating sp³–C (284.3 eV), C–C (285.7 eV), and C=O (288.2 eV) bonds.

To confirm the effect of AlF₃ coating on the sample morphology, the FE-SEM (Fig. 3(a–c)) analysis has been carried out for the LCMO@AlF₃. The agglomeration of the LCMO@AlF₃ particles leads to the formation of spherical particles, hence resulting in a non-uniform particle size distribution. The lattice fringe width has been evaluated from the area electron diffraction pattern (SAED), revealing the crystalline nature of the as-synthesized sample. The elemental mapping has been carried out

using an energy dispersive X-ray spectroscopy (EDS) (Fig. 3(g–j)), which exhibits a uniform distribution of elements such as Li, Mn, Co, O, Al, and F in the sample.

The structure and morphology of the as-synthesized LCMO@AlF₃ have been analyzed using FE-SEM and TEM imaging techniques. The FE-SEM shows a semi-uniform AlF₃ coating along with a non-uniform particle distribution. Also, from the TEM image (Fig. 3(d–f)), the inter-layer spacing has been calculated to be 0.25 nm, which can be assigned to the (311) crystal plane. In addition, the SAED pattern (Fig. 3(f)) further confirms the crystalline nature of the compound. The EDS mapping (Fig. 3(g–j)) also indicates the homogenous elemental distribution of Co, Mn, O, Al, and F in the compound.

3.1. Half-cell performance

To investigate the effect of AlF₃ coating on the electrochemical performance of LCMO, a preliminary half-cell study has been conducted in a voltage range of 3.5–5.2 V vs. Li/Li⁺ at a current density of 20 mA g^{−1}. The Galvanostatic charge-discharge (GCD) exhibits a superior electrochemical performance among the 1, 2, and 3 wt.% of AlF₃ with specific capacities of 107, 102, and 95 mAh g^{−1} and retentions of 68, 77, and 74% after 100 cycles, whereas the pristine LCMO exhibit poor electrochemical performance compared to LCMO@AlF₃ with a discharge capacity of 105 mAh g^{−1} with a capacity retention of 45% after 100 cycles (Fig. 4(a–b)). In addition, the rate performance study carried out at different current densities of 20–100 mA g^{−1} exhibits better electrochemical performance among the LCMO@AlF₃: 1–3 wt.% compared to that of pristine LCMO (Fig. 4(c–d)). This superior electrochemical performance of the LCMO@AlF₃ can be explained by the insertion of Li-ions from the electrolyte into the coating layer, which in turn converts AlF₃ to a stable Li_xAl_yF_z phase, hence providing an additional pathway for Li⁺ ion migration, thereby enhancing its ionic conductivity. Moreover, the thickness of AlF₃ coating plays a crucial role in the electrochemical performance of LCMO; hence, it is necessary to screen the optimal AlF₃ composition. Therefore, taking into account the GCD and the rate performance profiles, the optimum AlF₃ composition has been screened to be in the range of 2–3 wt.%.

The CV (Fig. 5) of the pristine LCMO and LCMO@AlF₃: 1–3 wt.% have been evaluated between 3.5 and 5.2 V vs. Li/Li⁺ at a scan rate of

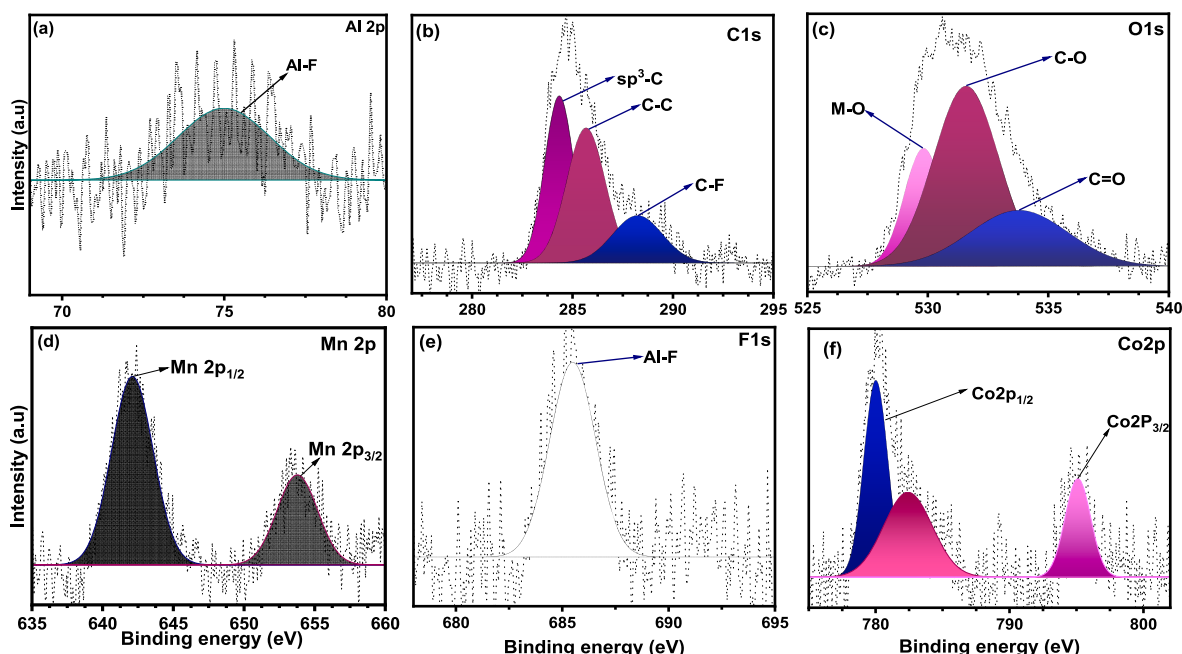


Fig. 2. (a) High-resolution XPS spectra of the as-synthesized LCMO@AlF₃ showing the elements present (b–f) XPS spectra of Al 2p, C 1s, O 1s, Mn 2p, F 1s and Co 2p.

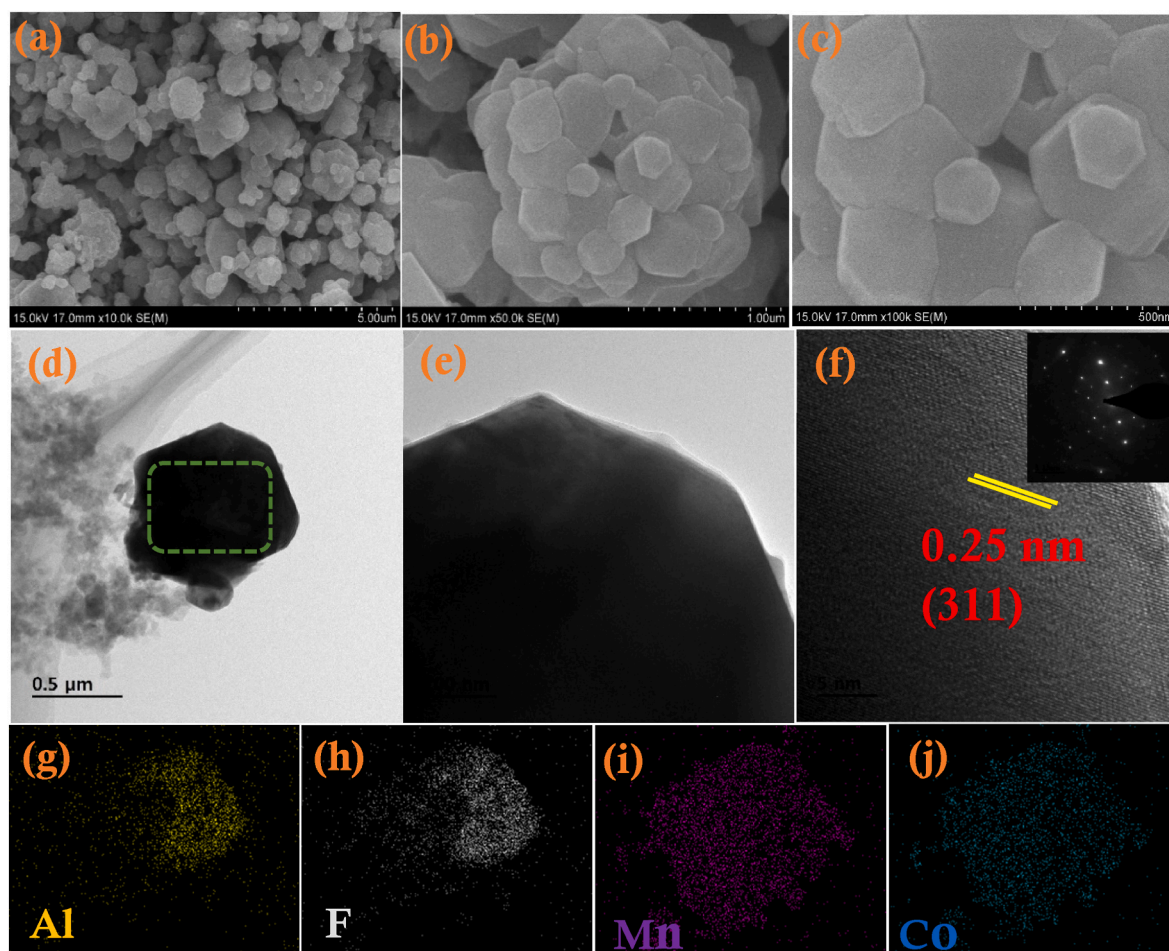


Fig. 3. (a–c) FE-SEM images of LCMO@AlF₃, (d–f) HR-TEM images of LCMO@AlF₃; Inset: SAED pattern, and (g–j) EDS elemental mapping of LCMO@AlF₃, showing the elemental distribution of Al, F, Mn, and Co.

0.1 mV s⁻¹. The two pairs of redox peaks indicate the presence of Co³⁺/Co²⁺ and Mn⁴⁺/Mn³⁺ couples and agree with the GCD profile. In addition, the reduction in the oxidation and reduction peak current has been observed as the composition of AlF₃ is increased from 1 to 3 wt.%, which can be accounted for by the decreased Li⁺ ion mobility with an increase in the thickness of the surface coating layer. Also, a shift in the oxidation and reduction peaks for the Co³⁺/Co²⁺ and Mn⁴⁺/Mn³⁺ couples can be observed as the AlF₃ coating on LCMO is increased from 1 to 3 wt.%, owing to the increase in polarization due to the Al–F bond present in the AlF₃. Hence, a rise in polarization is observed as the AlF₃ coating concentration increased from 1 to 3 wt.%.

To analyze the kinetics and mechanism of the Li⁺ ion transfer, electrochemical impedance spectroscopy (EIS) (Fig. 6(a–d)) has been performed for both pristine LCMO and LCMO@AlF₃: 1–3 wt.%. The Nyquist plot consists of two different regions, among which the semi-circle in the high-frequency region is attributed to the solution resistance (R_{Ω}) and the charge-transfer resistance (R_{CT}), whereas the low-frequency consists of the Warburg (Z_W) region. However, at moderate temperatures, the Nyquist plot comprises R_{Ω} , R_{CT} , constant phase element (Q), and Z_W ; meanwhile, at low temperatures, the freezing-up of electrolytes leads to poor Li⁺ ion diffusion; hence the Nyquist plot comprises only R_{Ω} , R_{CT} , and Q. Also, regardless of the applied temperatures, the Nyquist plots for both pristine and LCMO@AlF₃ reveal that the LCMO@AlF₃: 1 wt.% exhibit higher R_{CT} value compared to that of pristine LCMO, meanwhile as the AlF₃ composition is increased to 2 and 3 wt.% a drastic decrease in the R_{CT} value has been observed compared to that of LCMO and LCMO@AlF₃: 1 wt.% owing to the enhancement in the Li⁺ ion diffusion. Similarly, the R_{Ω} exhibits similarity in the trend as

that of R_{CT} , with a higher value of R_{Ω} for 1 wt.%, while low R_{CT} value has been observed among 2 and 3 wt.% AlF₃ coating, respectively. The Q refers to a capacitive term that indicates the double layer formation, hence the AlF₃ coating and SEI layer formation. Also, the constant phase elements Q₁, Q₂, and Q₃ mark the roughness of both SEI and AlF₃ layers.

In addition, the *in-situ* impedance analysis (Figure S3 (i–j)) reveals the formation of an SEI layer during the initial electrochemical cycling from the 1st to 10th cycle, which is accounted for by the dramatic increase in the R_{CT} value. On the contrary, as the cycling reaches the 50th cycle, the R_{CT} value remains almost stable, which marks the stability of the as-formed AlF₃ layer. But, a slight increase in the R_{CT} value has been observed at the 100th cycle due to the unfavorable side reactions and electrolyte decomposition.

The Li⁺ ion diffusion coefficient has been evaluated from both the EIS and CV plots. The diffusion coefficient from the Nyquist plot has been determined from the low-frequency Warburg region the slope of the Z vs. $\omega^{-1/2}$ plot (Fig. S5) using the equation [33–36].

$$D_{Li}^+ = R^2 T^2 / 2 A^2 n^4 F^4 \sigma_w^2 C^2$$

Where R is the universal gas constant (8.314 J K⁻¹ mol⁻¹), T is the temperature (298 K), A is the surface area of the electrode, n is the number of Li⁺ ions involved in charge-discharge, F is the Faraday constant (96,500 C mol⁻¹), σ_w is the slope of the curve, and C is the electrolyte concentration. As expected, an increase in the magnitude of D_{Li}^+ (Table T2) has been observed as the amount of AlF₃ is increased from 1 to 3 wt.% as 2.03×10^{-12} to 3.42×10^{-12} cm² s⁻¹ compared to that of pristine LCMO.

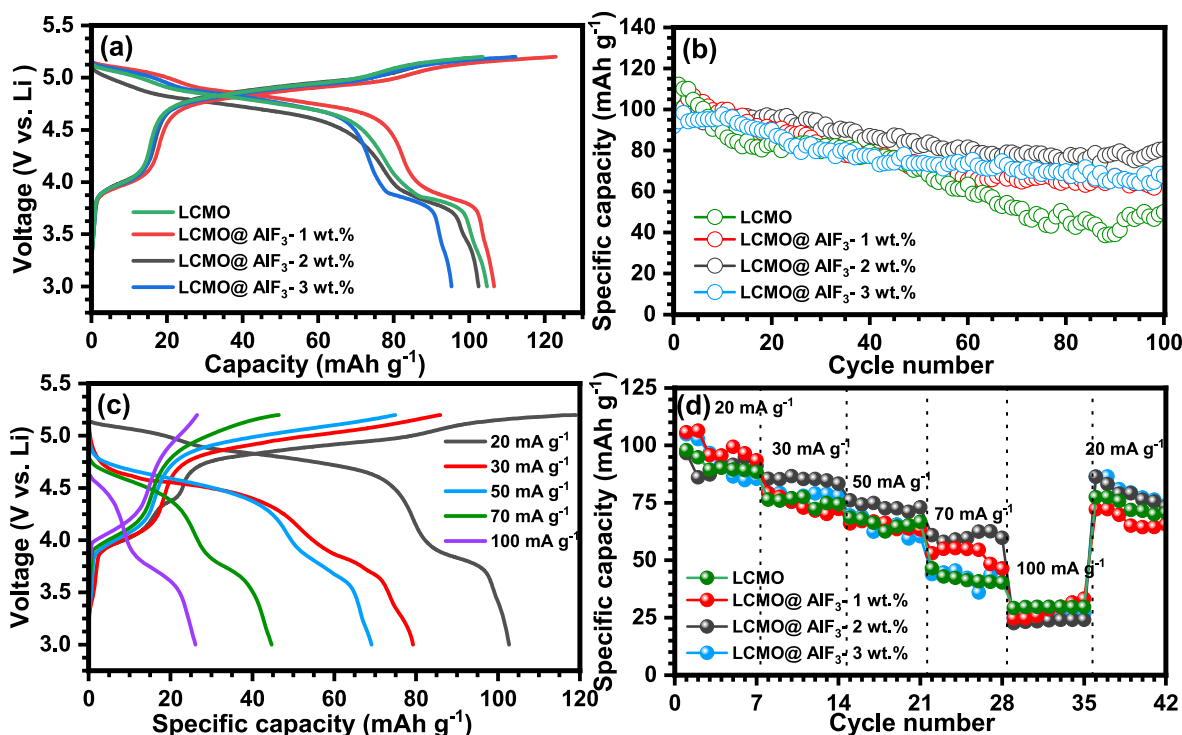


Fig. 4. (a) Galvanostatic charge-discharge curve, (b) specific capacity vs. cycle number plots of LCMO and LCMO@AlF₃: 1–3 wt.% at a current density of 20 mA g⁻¹, (c) charge-discharge curves of LCMO@AlF₃: 3 wt.% at current densities of 20, 30, 50, 70, and 100 mA g⁻¹, and (d) rate-performance study of LCMO and LCMO@AlF₃: 1–3 wt.%.

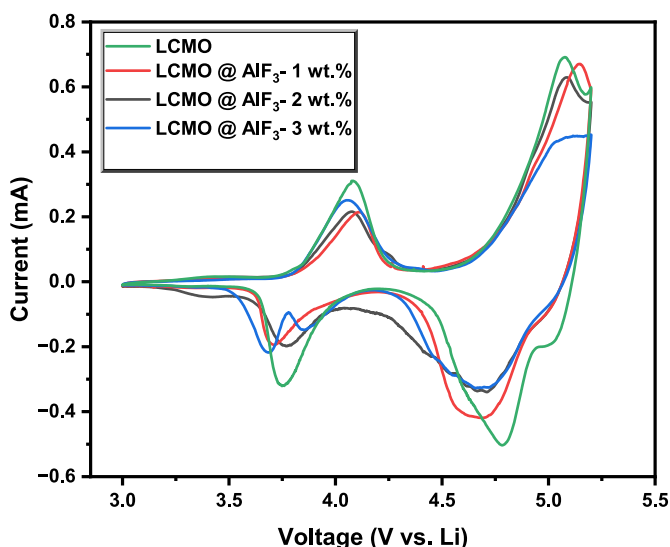


Fig. 5. Cyclic voltammetry curves of LCMO and LCMO@AlF₃: 1–3 wt.% at a scan rate of 0.1 mV s⁻¹.

The as-determined value of the diffusion coefficient from the EIS plot has been further verified from the CV, which is carried out at a scan rate of 0.1–1 mV s⁻¹. To determine the Li⁺ ion diffusion coefficient from CV, the slope of the I_p vs. $v^{1/2}$ graph (Fig. S4) has been determined, followed by its calculation from the Randles-Sevcik equation [36,37].

$$I_p = 2.69 \times 10^5 n^{3/2} C_0 A D^{1/2} v^{1/2}$$

Where I_p is the peak current (anodic or cathodic), C_0 is the concentration of electrolytes, A is the cross-section area of the electrode, D is the Li⁺ ion diffusion coefficient, and v is the scan rate. The calculated value of the diffusion coefficients (Table T1) exhibits a rise in their magnitude from

LCMO@AlF₃ – 1 wt.% to LCMO@AlF₃ – 3 wt.%, along with a fall in their magnitude among the pristine LCMO. Thus, a correlation in the trend can be observed among the diffusion coefficients calculated from both the CV and the EIS analysis.

To determine the feasibility of the electrochemical reaction, a comparison based on the activation energy of the as-synthesized pristine LCMO and LCMO@AlF₃: 1–3 wt.% have been carried out from the Arrhenius plot. The evaluation of activation energy has been done from the slope of $\ln(\sigma)$ vs. $1000/T$ plot (Fig. S6) using the equation-

$$\ln(\sigma) = \ln(\sigma_0) - E_a / 1000RT$$

Where σ is the conductance, σ_0 is the pre-exponential factor, and E_a is the activation energy (eV). Based on the calculation (Table T3), the activation energy decreased from 0.33 to 0.23 eV from pristine LCMO to LCMO@AlF₃: 3 wt.%. Hence, an enhancement in the Li⁺ ion kinetics can be observed as the amount of AlF₃ increases from 1 to 3 wt.% compared to that of pristine LCMO. Therefore, the trend in activation energy for both LCMO and LCMO@AlF₃: 1–3 wt.% agree with the diffusion coefficient calculated from the CV and EIS.

An *in-operando* powder XRD analysis (Fig. 7) has been carried out to investigate the phase change and the structure of the LCMO during charge-discharge between 3.5 and 5.2 V vs. Li/Li⁺. The *in-operando* XRD exhibits a shift in the 2 θ value as the charge-discharge progresses, which indicates the expansion and contraction of the cubic unit cell during the Li⁺ ion insertion and extraction. Adding to this, the LCMO undergoes a solid-solution mechanism without any phase change during the entire charge-discharge process, which has also been proven from the *in-operando* XRD analysis [34,38–40].

Although the spinels undergo a two-phase mechanism, the small cation size difference between Mn³⁺/Mn⁴⁺ and Co³⁺/Co⁴⁺ during the Li⁺ ion insertion and extraction process will favor the occurrence of a solid-solution mechanism.

The nature of the as-formed AlF₃ coating has been analyzed by conducting a post-mortem analysis of both cycled and uncycled

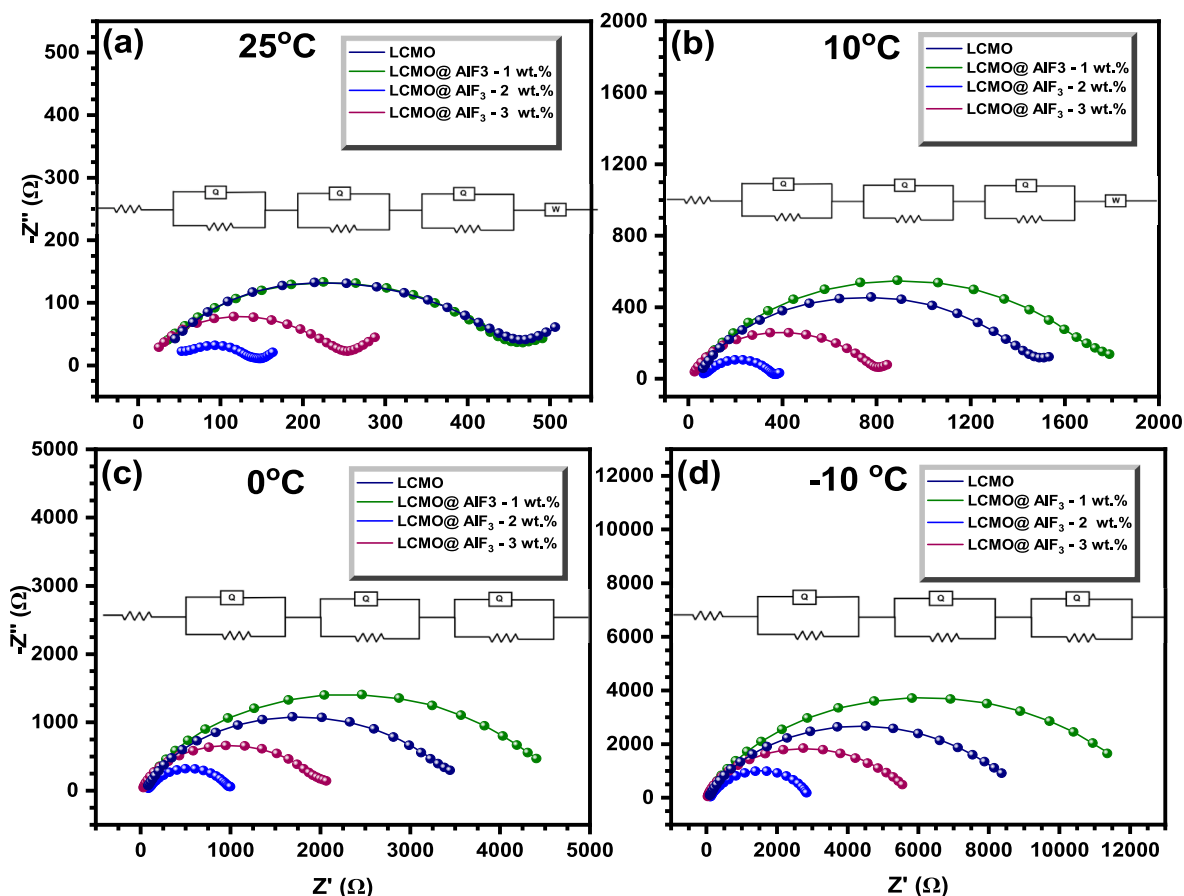


Fig. 6. (a–d) Nyquist plots of LCMO and LCMO@AlF₃: 1–3 wt.% at different temperatures ranging from –10 to 25 °C along with their corresponding equivalent circuits at a frequency ranging from 0.1 Hz to 10 kHz.

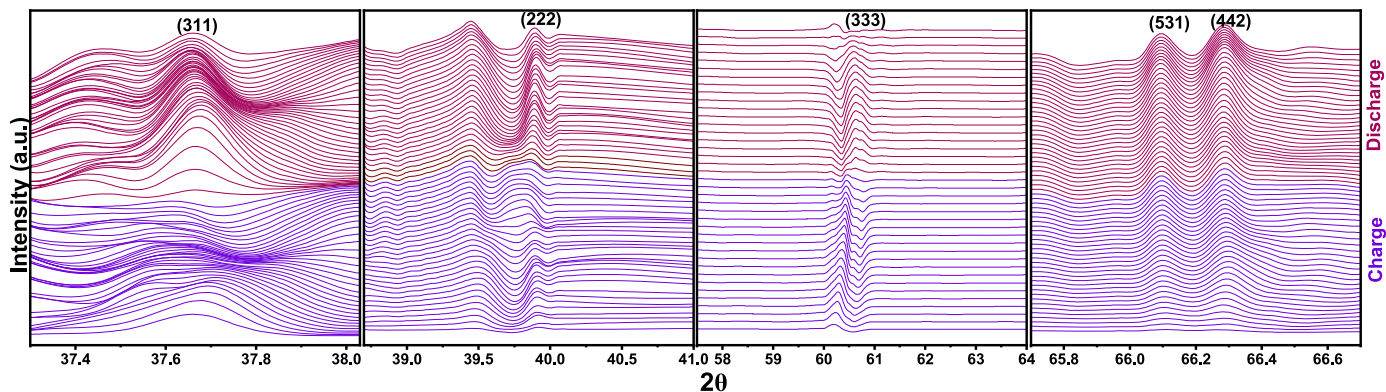


Fig. 7. In-situ XRD analysis of LCMO@AlF₃.

electrodes [41]. The powder XRD (Fig. S7) analysis of the cycled and uncycled electrode reveals the fact that the cubic crystal structure of the LCMO lattice has been maintained after the charge-discharge, which is attributed to the absence of any peak shift. In addition, the absence of diffraction peaks corresponding to the side products such as Li₂CO₃ or LiF can be attributed to the absence of any parasitic side reactions, thereby enhancing the cycle stability as well as the rate capability of LCMO. The elemental surface distribution of both cycled and uncycled electrodes was determined from the XPS analysis (Fig. S8). The F 1s XPS spectra of both electrodes exhibit a broad single peak corresponding to C–F (689.8 eV). However, no change in the C–F peak intensity for both electrodes suggests the absence of parasitic side reactions leading to the formation of LiF, Li₂CO₃, etc., hence showing the stability of the

as-formed AlF₃ coating. In addition, the peaks corresponding to the O 1s core level can be assigned to M(Co/Mn)–O (529 eV), C–O (531 eV), and C=O (532.8 eV) bonds. Also, the similar peak intensity of the M (Co/Mn)–O bond for both electrodes indicates the absence of metal ion dissolution, hence making it clear that the uniform AlF₃ coating on LCMO prevents it from direct contact with the electrolyte, thereby mitigating the parasitic reactions of the electrode with electrolyte.

The FE-SEM (Fig. S9) images reveal the morphology and nature of the AlF₃ surface layer for the cycled and uncycled electrodes. The FE-SEM images of cycled and uncycled electrodes exhibit particle agglomeration, leading to its agglomeration, resulting in an irregular particle size distribution. The FE-SEM pictures further illustrate a uniform AlF₃ coating among the uncycled electrodes. However, owing to the

electrolyte decomposition and SEI layer formation, a non-uniform AlF_3 coating can be observed among the cycled electrodes. Thus, from the FE-SEM image, it can be concluded that as the cycling progresses, the SEI layer gets disrupted, which leads to the consumption of more Li^+ ions, hence causing irreversibility and poor cycle stability.

3.2. Full-cell performance

The full-cell assembly is fabricated with the spinel anode, LTO, with LCMO and LCMO@AlF_3 :2–3 wt.% cathodes under balanced loading conditions. The full-cell assembly was tested in a 1.5–3.7 V voltage range at a constant current density of 20 mA g^{-1} . The full-cell renders 48, 83, and 66% of initial capacity after 80 cycles (Fig. 8(a–b)) with initial discharge capacities of 96, 94, and 95 mAh g^{-1} for LCMO/LTO, LCMO@AlF_3 :2 wt.%/LTO, and LCMO@AlF_3 :3 wt.%/LTO assemblies, respectively. Apparently, the AlF_3 coating dilutes the undesirable side reactions with electrolyte, which translates to better cycling stability and rate capability for LCMO@AlF_3 :2–3 wt.%/LTO configuration compared to LCMO/LTO.

The temperature-dependent electrochemical activity (Fig. 8(c–d)) of both the LCMO@AlF_3 :2 wt.%/LTO and LCMO@AlF_3 :3 wt.%/LTO assemblies are subjected to various temperature conditions ranging from -10 to 20°C . At low-temperature conditions (0 and -10°C), the full-cell exhibits poor electrochemical performance due to the freezing-up of electrolyte solution, resulting in sluggish Li-ion kinetics. However, at moderate temperatures (10 and 20°C), the increased Li-ion mobility caused due to thermal agitation results in an enhancement in the electrochemical performance.

4. Conclusion

The LCMO has been synthesized by a co-precipitation method followed by a wet AlF_3 coating from 1 to 3 wt.%. However, the AlF_3 coating does not influence the crystal structure and the electrochemical charge-discharge of LCMO. In addition, the GCD profile exhibits excellent

electrochemical performance among the LCMO@AlF_3 compared to that of pristine LCMO, owing to the strong Al–F bond, which enhances the Li^+ ion conductivity. Further, the optimal AlF_3 coating on the LCMO has been screened to be in the range of 2–3 wt.%. The diffusion coefficient calculated from both CV and EIS exhibits a similar trend with a proportional rise in diffusion coefficient as the AlF_3 coating increases from 1 to 3 wt.%. The Arrhenius plot exhibits a decreasing trend in the activation energy, hence validating the trend in the diffusion coefficient obtained from both CV and EIS. Also, the *in-operando* powder XRD marks the occurrence of a solid-solution mechanism without any phase change during the entire charge-discharge process. The full-cell study exhibits specific capacities of 94 and 95 mAh g^{-1} with retention of 83 and 66% after 80 cycles among the LCMO@AlF_3 :2 wt.%/LTO, and LCMO@AlF_3 :3 wt.%/LTO assemblies. In addition, the temperature study of both LCMO@AlF_3 :2 wt.%/LTO and LCMO@AlF_3 :3 wt.%/LTO exhibits better electrochemical performance at moderate temperatures of 10 and 20°C owing to the fast Li^+ ion transport due to thermal agitation. However, at low temperatures of 0 and -10°C due to the freezing-up of electrolytes, a sluggish Li^+ ion mobility has been observed, thereby leading to poor electrochemical performance. From a future perspective, the research on high-voltage cathodes should be extended to other cathodes such as LiCoPO_4 , $\text{LiNi}_{0.5}\text{Mn}_{1.5}\text{O}_4$, etc. Also, morphological modification using conductive polymers such as PEDOT, PANI, etc., must be explored further. In addition, electrolyte optimization using additives, development of solid electrolytes, etc., are some research areas requiring much attention.

CRediT authorship contribution statement

Sreekumar Sreedeeep: Conceptualization, Investigation, Resources, Writing – original draft. **Yun-Sung Lee:** Resources, Supervision, Funding acquisition. **Vanchiappan Aravindan:** Conceptualization, Resources, Writing – original draft, Supervision, Funding acquisition.

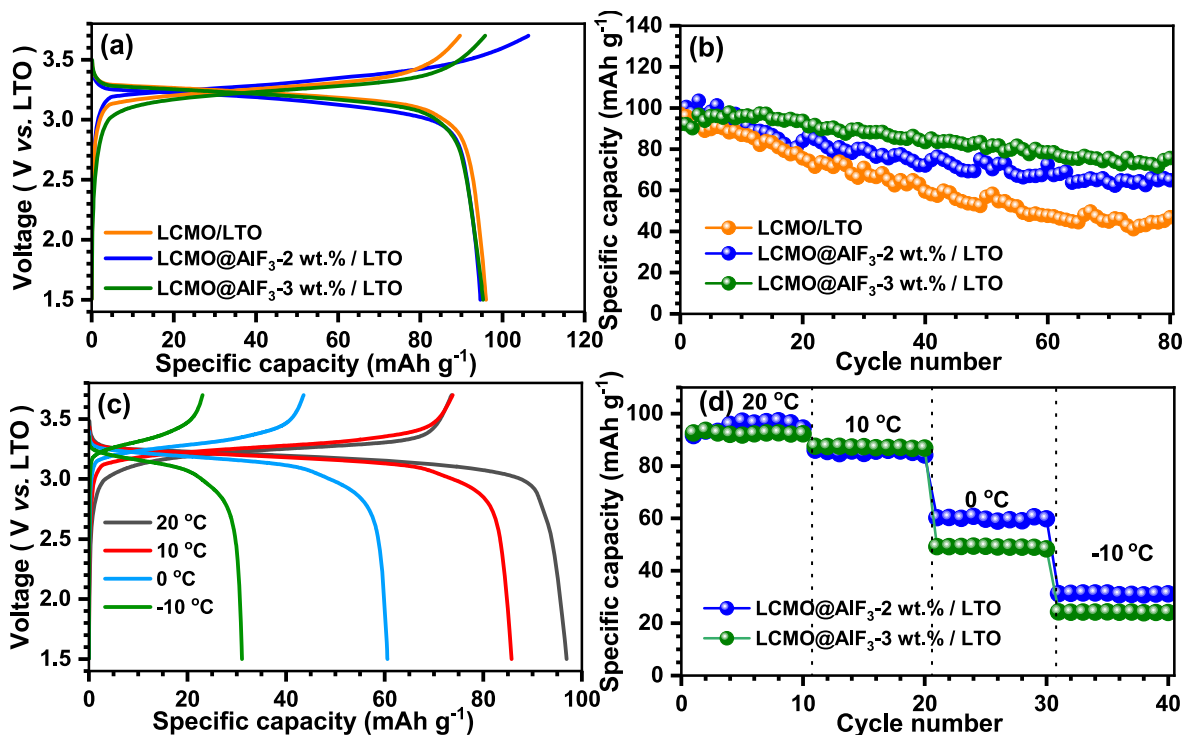


Fig. 8. (a) Charge-discharge curves, (b) specific capacity vs. cycle number of LCMO-LTO and LCMO@AlF_3 :2–3 wt.%/LTO full-cells at a current density of 20 mA g^{-1} within a voltage window of 1.5–3.7 V, (c) charge-discharge curve of LCMO@AlF_3 : 2–3 wt.%/LTO at different temperatures ranging from -10 to 20°C , and (d) specific capacity vs. cycle number.

Declaration of competing interest

The authors declare that they have no known competing financial interests or personal relationships that could have appeared to influence the work reported in this paper.

Data availability

Data will be made available on request.

Acknowledgement

SS acknowledges the Council of Scientific and Industrial Research (CSIR), Govt. of India for the fellowship. YSL acknowledges the financial support from the National Research Foundation of Korea (NRF) grant funded by the Korean government (Ministry of Science, ICT&Future Planning) (No. RS-2023-00208361). VA acknowledges financial support from the Science and Engineering Research Board (SERB), a statutory body of the Department of Science and Technology, Govt. of India, through the Swarnajayanti Fellowship (SB/SJF/2020–21/12).

Appendix A. Supplementary data

Supplementary data to this article can be found online at <https://doi.org/10.1016/j.compositesb.2024.111365>.

References

- Chen Y, Kang Y, Zhao Y, Wang L, Liu J, Li Y, Liang Z, He X, Li X, Tavajohi N, et al. A review of lithium-ion battery safety concerns: the issues, strategies, and testing standards. *J Energy Chem* 2021;59:83–99. <https://doi.org/10.1016/j.jchem.2020.10.017>.
- Tian Y, Zeng G, Rutt A, Shi T, Kim H, Wang J, Koettgen J, Sun Y, Ouyang B, Chen T, et al. Promises and challenges of next-generation “beyond Li-ion” batteries for electric vehicles and grid decarbonization. *Chem Rev* 2021;121(3):1623–69. <https://doi.org/10.1021/acs.chemrev.0c00767>.
- Opitz A, Badami P, Shen L, Vignarooban K, Kannan AM. Can Li-ion batteries Be the panacea for automotive applications? *Renew Sustain Energy Rev* 2017;68:685–92. <https://doi.org/10.1016/j.rser.2016.10.019>.
- Shahjalal M, Roy PK, Shams T, Fly A, Chowdhury JI, Ahmed MR, Liu K. A review on second-life of Li-ion batteries: prospects, challenges, and issues. *Energy* 2022;241:122881. <https://doi.org/10.1016/j.energy.2021.122881>.
- Natarajan S, Aravindan V. Burgeoning prospects of spent lithium-ion batteries in multifarious applications. *Adv Energy Mater* 2018;8(33):1–16. <https://doi.org/10.1002/aenm.201802303>.
- Deng D. Li-ion batteries: basics, progress, and challenges. *Energy Sci Eng* 2015;3(5):385–418. <https://doi.org/10.1002/ese3.95>.
- Nitta N, Wu F, Lee JT, Yushin G. Li-ion battery materials: present and future. *Mater Today* 2015;18(5):252–64. <https://doi.org/10.1016/j.mattod.2014.10.040>.
- Sreedeeep S, Natarajan S, Aravindan V. Recent advancements in LiCoPO₄ cathodes using electrolyte additives. *Curr Opin Electrochem* 2022;31:100868. <https://doi.org/10.1016/j.coelec.2021.100868>.
- Kumar PR, Madhusudhan Rao V, Nageswararao B, Venkateswarlu M, Satyanarayana N. Enhanced electrochemical performance of carbon-coated LiMPO₄ (M = Co and Ni) nanoparticles as cathodes for high-voltage lithium-ion battery. *J Solid State Electrochem* 2016;20(7):1855–63. <https://doi.org/10.1007/s10008-016-3151-5>.
- Goriparti S, Miele E, De Angelis F, Di Fabrizio E, Piroietti Zaccaria R, Capiglia C. Review on recent progress of nanostructured anode materials for Li-ion batteries. *J Power Sources* 2014;257:421–43. <https://doi.org/10.1016/j.jpowsour.2013.11.103>.
- Di Lecce D, Hassoun J. Lithium metal battery using LiFe_{0.5}Mn_{0.5}PO₄ olivine cathode and pyrrolidinium-based ionic liquid electrolyte. *ACS Omega* 2018;3(8):8583–8. <https://doi.org/10.1021/acsomega.8b01328>.
- Chen L, Fan X, Hu E, Ji X, Chen J, Hou S, Deng T, Li J, Su D, Yang X, et al. Achieving high energy density through increasing the output voltage: a highly reversible 5.3 V battery. *Chem* 2019;5(4):896–912. <https://doi.org/10.1016/j.chempr.2019.02.003>.
- Hu M, Tian Y, Wei J, Wang D, Zhou Z. Porous hollow LiCoMnO₄ microspheres as cathode materials for 5 V Lithium ion batteries. *J Power Sources* 2014;247:794–8. <https://doi.org/10.1016/j.jpowsour.2013.09.038>.
- Kreder KJ, Manthiram A. Vanadium-substituted LiCoPO₄ core with a monolithic LiFePO₄ shell for high-voltage lithium-ion batteries. *ACS Energy Lett* 2017;2(1):64–9. <https://doi.org/10.1021/acseenergylett.6b00496>.
- Park H, Manthiram A. Ethanothral synthesis of octahedral-shaped doped Mn₂O₃ single crystals as a precursor for LiMn₂O₄ spinel cathodes in lithium-ion batteries. *J Phys Chem C* 2023;127(18):8515–22. <https://doi.org/10.1021/acs.jpcc.3c02468>.
- Yu X, Yu WA, Manthiram A. Advances and prospects of high-voltage spinel cathodes for lithium-based batteries. *Small Methods* 2021;5(5):2001196. <https://doi.org/10.1002/smt.202001196>.
- Huang Z-X, Gu Z-Y, Heng Y-L, Huixiang Ang E, Geng H-B, Wu X-L. Advanced layered oxide cathodes for sodium/potassium-ion batteries: development, challenges and prospects. *Chem Eng J* 2023;452:139438. <https://doi.org/10.1016/j.cej.2022.139438>.
- Huang Z-X, Zhang X-L, Zhao X-X, Heng Y-L, Wang T, Geng H, Wu X-L. Hollow Na_{0.62}K_{0.05}Mn_{0.7}Ni_{0.2}Co_{0.1}O₂ polyhedra with exposed stable {001} facets and K riveting for sodium-ion batteries. *Sci China Mater* 2023;66(1):79–87. <https://doi.org/10.1007/s40843-022-2157-8>.
- Reeves-McLaren N, Hong M, Alqurashi H, Xue L, Sharp J, Rennie AJ, Boston R. The spinel LiCoMnO₄: 5 V cathode and conversion anode. *Energy Proc* 2018;151:158–62. <https://doi.org/10.1016/j.egypro.2018.09.041>.
- Laszczynski N, Birrozzi A, Maranski K, Copley M, Schuster ME, Passerini S. Effect of coatings on the green electrode processing and cycling behaviour of LiCoPO₄. *J Mater Chem A* 2016;4(43):17121–8. <https://doi.org/10.1039/c6ta05262b>.
- Gangulibabu, Nallathambi K, Meyrick D, Minakshi M. Carbonate anion controlled growth of LiCoPO₄/C nanorods and its improved electrochemical behavior. *Electrochim Acta* 2013;101:18–26. <https://doi.org/10.1016/j.electacta.2012.09.115>.
- Liu J, Conry TE, Song X, Yang L, Doeff MM, Richardson TJ. Spherical nanoporous LiCoPO₄/C composites as high performance cathode materials for rechargeable lithium-ion batteries. *J Mater Chem* 2011;21(27):9984–7. <https://doi.org/10.1039/c1jm10793c>.
- Sreedeeep S, Aravindan V. Fabrication of 4.7 V class “rocking-chair” type Li-ion cells with carbon-coated LiCoPO₄ as cathode and graphite anode. *Mater Lett* 2021;291:1–4. <https://doi.org/10.1016/j.matlet.2021.129609>.
- Kwon Y, Lee Y, Kim SO, Kim HS, Kim KJ, Byun D, Choi W. Conducting polymer coating on a high-voltage cathode based on soft chemistry approach toward improving battery performance. *ACS Appl Mater Interfaces* 2018;10(35):29457–66. <https://doi.org/10.1021/acsami.8b08200>.
- Yoon Y, Shin S, Shin MW. Fundamental understanding of the effect of a polyaniline coating layer on cation mixing and chemical states of LiNi_{0.9}Co_{0.085}Mn_{0.015}O₂ for Li-ion batteries. *ACS Appl Polym Mater* 2023;5(2):1344–53. <https://doi.org/10.1021/acsapm.2c01872>.
- Zhao T, Li L, Chen R, Wu H, Zhang X, Chen S, Xie M, Wu F, Lu J, Amine K. Design of surface protective layer of LiF/FeF₃ nanoparticles in Li-rich cathode for high-capacity Li-ion batteries. *Nano Energy* 2015;15:164–76. <https://doi.org/10.1016/j.nanoen.2015.04.013>.
- Lee HJ, Park YJ. Synthesis of Li[Ni_{0.2}Li_{0.2}Mn_{0.6}]O₂ nano-particles and their surface modification using a polydopamine layer. *J Power Sources* 2013;244:222–33. <https://doi.org/10.1016/j.jpowsour.2013.01.154>.
- Tron A, Park YD, Mun J. AlF₃-Coated LiMn₂O₄ as cathode material for aqueous rechargeable Lithium battery with improved cycling stability. *J Power Sources* 2016;325:360–4. <https://doi.org/10.1016/j.jpowsour.2016.06.049>.
- Wu Q, Yin Y, Sun S, Zhang X, Wan N, Bai Y. Novel AlF₃ surface modified spinel LiMn_{1.5}Ni_{0.5}O₄ for lithium-ion batteries: performance characterization and mechanism exploration. *Electrochim Acta* 2015;158:73–80. <https://doi.org/10.1016/j.electacta.2015.01.145>.
- Sharabi R, Markevich E, Borgel V, Salitra G, Gershinshy G, Aurbach D, Semrau G, Schmidt MA, Schall N, Stinner C. Raman study of structural stability of LiCoPO₄ cathodes in LiPF₆ containing electrolytes. *J Power Sources* 2012;203:109–14. <https://doi.org/10.1016/j.jpowsour.2011.12.018>.
- Kang YM, Kim Y II, Oh MW, Yin RZ, Lee Y, Han DW, Kwon HS, Kim JH, Ramanath G. Structurally stabilized olivine Lithium phosphate cathodes with enhanced electrochemical properties through Fe doping. *Energy Environ Sci* 2011;4(12):4978–83. <https://doi.org/10.1039/c1ee02283k>.
- Lai CH, Ashby DS, Lin TC, Lau J, Dawson A, Tolbert SH, Dunn BS. Application of poly(3-hexylthiophene-2,5-diyl) as a protective coating for high rate cathode materials. *Chem Mater* 2018;30(8):2589–99. <https://doi.org/10.1021/acs.chemmater.7b05116>.
- Nguyen TQ, Breitkopf C. Determination of diffusion coefficients using impedance spectroscopy data. *J Electrochem Soc* 2018;165(14):E826–31. <https://doi.org/10.1149/2.1151814jes>.
- Kosova NV, Podgornova OA, Devyatkina ET, Podugolnikov VR, Petrov SA. Effect of Fe²⁺ substitution on the structure and electrochemistry of LiCoPO₄ prepared by mechanochemically assisted carbothermal reduction. *J Mater Chem A* 2014;2(48):20697–705. <https://doi.org/10.1039/c4ta04221b>.
- Zhang D, Zhou J, Chen J, Xu B, Qin W, Chang C. Rapid synthesis of LiCo_{1-x}Fe_xPO₄/C cathodes via microwave solvothermal method for Li-ion batteries. *Int J Electrochem Sci* 2018;13(3):2544–55. <https://doi.org/10.20964/2018.03.61>.
- Wu X, Meledina M, Tempel H, Kungl H, Mayer J, Eichel R. Morphology-controllable synthesis of LiCoPO₄ and its influence on electrochemical performance for high-voltage Lithium ion batteries. *J Power Sources* 2020;450(October 2019):227726. <https://doi.org/10.1016/j.jpowsour.2020.227726>.
- Wu X, Meledina M, Barthel J, Liu Z, Tempel H, Kungl H, Mayer J, Eichel RA. Investigation of the Li–Co antisite exchange in Fe-substituted LiCoPO₄ cathode for high-voltage Lithium ion batteries. *Energy Storage Mater* 2019;22(March):138–46. <https://doi.org/10.1016/j.ensm.2019.07.004>.
- Strobridge FC, Liu H, Leskes M, Borkiewicz OJ, Wiaderek KM, Chupas PJ, Chapman KW, Grey CP. Unraveling the complex delithiation mechanisms of olivine-type cathode materials, LiFe_xCo_{1-x}PO₄. *Chem Mater* 2016;28(11):3676–90. <https://doi.org/10.1021/acs.chemmater.6b00319>.

- [39] Zhu W, Liu D, Gagnon C, Gariépy V, Trudeau ML, Vijh A, Zaghib K. Phase transformation of doped LiCoPO_4 during galvanostatic cycling. *Materials* 2020;13 (17). <https://doi.org/10.3390/ma13173810>.
- [40] Manzi J, Vitucci FM, Paolone A, Trequattrini F, Di Lecce D, Panero S, Brutti S. Analysis of the self-discharge process in LiCoPO_4 electrodes: bulks. *Electrochim Acta* 2015;179:604–10. <https://doi.org/10.1016/j.electacta.2015.03.071>.
- [41] Kim T, Ono LK, Qi Y. Elucidating the mechanism involved in the performance improvement of lithium-ion transition metal oxide battery by conducting polymer. *Adv Mater Interfac* 2019;6(7):1–13. <https://doi.org/10.1002/admi.201801785>.